1-1-2016

Potential of Unmanned Aerial Systems Imagery Relative to Landsat 8 Imagery in the Lower Pearl River Basin

John William Van Horn

Potential of Unmanned Aerial Systems imagery relative to Landsat 8 imagery in the Lower Pearl River Basin

By

John William Van Horn III

A Thesis
Submitted to the Faculty of
Mississippi State University
in Partial Fulfillment of the Requirements
for the Degree of Master of Science
in Geosciences
in the Department of Geosciences

Mississippi State, Mississippi

December 2016

Potential of Unmanned Aerial Systems imagery relative

to Landsat 8 imagery in the Lower

Pearl River Basin

By

John William Van Horn III

Approved:

_____

Jamie L. Dyer
(Director of Thesis)

_____

Andrew E. Mercer
(Committee Member)

_____

Padmanava Dash
(Committee Member)

_____

Michael E. Brown
(Graduate Coordinator)

_____

Rick Travis
Interim Dean
College of Arts & Sciences

Name: John William Van Horn III

Date of Degree: December 9, 2016

Institution: Mississippi State University

Major Field: Geosciences

Director of Thesis: Jamie Dyer

Title of Study: Potential of Unmanned Aerial Systems imagery relative to Landsat 8 imagery in the Lower Pearl River Basin

Pages in Study 43

Candidate for Degree of Master of Science

Hurricane Isaac's landfall on the coast of Louisiana spawned a hydrological research project between Mississippi State University (MSU), the Northern Gulf Institute (NGI), and the National Oceanic and Atmospheric Administration (NOAA) in the Lower Pearl River Basin (LPRB). Unmanned aerial systems data collection missions were scheduled every two months in the LPRB. This research provides a comparison between Landsat-8 imagery and corresponding UAS imagery with regards to the four remote sensing resolutions: spatial, spectral, radiometric, and temporal. Near-infrared (NIR) imagery from each platform was compared by land-water masks and statistical comparisons. A classification method known as natural breaks with Jenks Optimization determined threshold values between land and water for each image. Land-water masks revealed substantial differences between areas of land and water in comparing imagery. The overall difference in average land and water percentages between the two platforms was 1.77%; however, a larger percentage was 20.41% in a single comparison.

TABLE OF CONTENTS

LIST OF TABLES

LIST OF FIGURES

CHAPTER I

INTRODUCTION / BACKGROUND

1.1 Research Initiative and Study Area

The growing reputation and potential applications of UASs are evident through the expanding use by environmental agencies and research organizations. For example, a workshop held in Boulder, CO in February of 2012 initiated the integration of UASs for National Weather Service (NWS) River Forecast Centers (RFCs) regarding river and levee requirements. The workshop encouraged the attendance of vendors or operators of UAS platforms and sensors, and service providers. One of the main requirements discussed in this workshop was the rapid response after a catastrophic flooding event to track changes in river channel structure and morphology in an attempt to quickly update river models (Moorhead, et al. 2012). The goals of the Boulder workshop were coincidently reassured by the hurricane season of 2012, where Alabama, Louisiana, and Mississippi coastal RFCs were challenged by inundation caused by Hurricane Isaac.

Areas along the Louisiana and Mississippi coasts experienced excessive amounts of storm total rainfall during Hurricane Isaac, ranging from 525 mm (20.66 in) in New Orleans, LA to 10.39 inches in Slidell, LA. Total inundation amounts around the Highway 90 (Pearl River boat launch) topped out at 1.8 m with a storm tide of over 2.7 m along with heavy rains (NOAA Tropical Cyclone Report 2013). The combination of heavy rains, storm surge, and storm tide were powerful enough to force a section of the

Mississippi River to flow backwards for a 24-hour period (NOAA Tropical Cyclone Report 2013). Flooding was imminent along the central Gulf States during Hurricane Isaac, but the aftermath created lasting inundation around lower Louisiana and Mississippi. More specifically, the Lower Pearl River Basin (LPRB) below Highway 90 experienced areas that remained inundated well after Hurricane Isaac's existence.

Following the flooding conditions caused by Hurricane Isaac in 2012, the NWS RFCs along the Mississippi and Louisiana Gulf Coast initiated a NOAA-backed research grant to locate inundation within areas of sparse river gauges along the LPRB. The focal area of interest negotiated by RFCs was the Lower Pearl River Basin. An image of the study area is shown in Figure 1.1, which will be referred to in this research as the 'localized research parameter'.

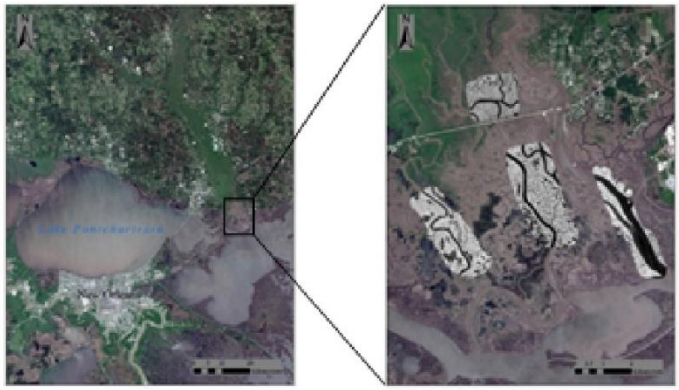

Figure 1.1 Localized Research Parameter

(a) January 6th, 2015 Landsat-8 true-color imagery of Lake Pontchartrain and the New Orleans area, and (b) the localized research parameter in the Lower Pearl River Basin with UASs NIR focal-imagery overlay.

1.2 Remote Sensing

Remote sensing applications have expanded greatly since the early-1900s; during an era in which advancements in technology were driven mainly by military agendas. Additionally, global remote sensing became relevant following the birth of satellite technology in the late 1950s. In fact, the term 'remote sensing' was not introduced until 1960 by U.S. Office of Naval Research personnel, long after both world wars (Jensen 2007). Since the popularization of remote sensing by military operations and space exploration, the applications have become quite vast within the geosciences field.

In the late 1980s, the American Society for Photogrammetry and Remote Sensing (ASPRS) combined the definitions of photogrammetry and remote sensing into the art, science, and technology of obtaining reliable information about the physical objects and the environment, through the process of recording, measuring and interpreting imagery and digital representations of energy patterns derived from non-contact sensor systems (Colwell 1997). A modern explanation, according to Schmugge et al. (2002), is that remote sensing is the process of inferring surface parameters from measurements of the upwelling electromagnetic radiation from the land surface. This radiation is both reflected and emitted by the land. Both definitions highlight and express the potential of remote sensing technologies in the environment. In other words, remote sensing is a cost-effective, time-efficient tool to systematically and periodically provide coverage of inaccessible regions (Dash et al. 2002).

Due to a vast array of technology that remote sensing entails, a mention of the distance at which an object is measured should be addressed. Such extremes can be exemplified by a satellite, such as Landsat-8, which remote senses from an orbital

location, or Unmanned Aerial Systems (UASs) that collect data from a few hundred meters above the lithosphere. Both examples are well-documented in the field of remote sensing, and reflect the stated definitions from Colwell (1997), Schmugge et al. (2002) and Dash et al. (2002). A wide variety of remote sensing technologies are readily available for operational use depending on the desired data sought. Major factors, such as the type of resolution used in imaging, must be considered for collecting data.

1.2.1 Spatial Resolution

Spatial resolution can be described as the measurement of the smallest angular or linear separation between two objects that can be resolved by the remote sensing system (Jensen 2007). Spatial resolution defines the size of the pixels of a measured object within the instantaneous-field-of-view (IFOV) of the remote sensing sensor. For an example, Figure 1.2 presents a subject ground area of 1.8×10^4 m^2 that was aerial imaged by 30 m and 0.05 m spatial resolution platforms. The 30 m spatial resolution platform contains a total of 20 pixels to represent the NIR image; whereas the 0.05 m spatial resolution platform of the exact NIR image contains a total of 3.60×10^5 pixels. According to Jenson 2007, the required spatial resolution for adequate imaging is at least one-half of the object measured in its smallest dimension. In the example of Figure 1.2, the 0.05 m platform is considered fine spatial resolution when compared to the 30 m platform's coarse spatial resolution. The former is referred to as 'high spatial resolution' and the latter is said to have 'low spatial resolution'.

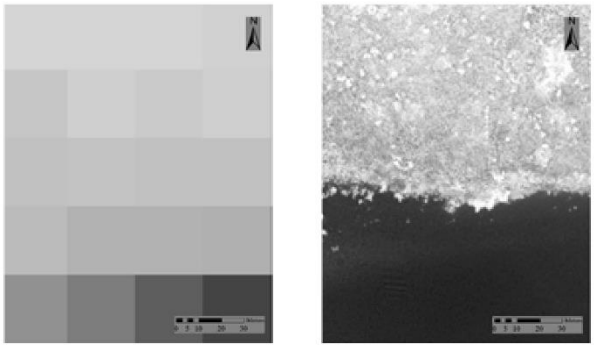

Figure 1.2 Spatial Resolution Difference

NIR imagery displaying the spatial resolution difference between (a) 30 m and (b) 0.05 m of the exact area of 1.80 x 10^4 m^2.

1.2.2 Spectral Resolution

Spectral resolution refers to the amount and dimensions of wavelength intervals in the electromagnetic spectrum, (known as 'bands' or 'channels'), that the remote sensing equipment can measure (Jensen 2007). For example, Landsat-5's Multispectral Scanner (MSS) imaged in 4 bands, opposed to the 7 bands that are imaged from the Enhanced Thematic Mapper Plus (ETM^+) on Landsat-7. Typically, spectral resolution is separated into: broadband (visible, shortwave infrared, and longwave infrared bands), multispectral (several bands), hyperspectral (hundreds of bands), and ultraspectral (hundreds to thousands of bands). Multispectral resolution has a higher spectral resolution than a broadband platform, but a lower spectral resolution than a hyperspectral.

Another main aspect of spectral resolution is the calibrated bandwidth of each band. These calibrations are intended to optimize each band for the desired data to be collected from the remote sensing platform. For an example, the Landsat-7 ETM^+ has a near-infrared (NIR) bandwidth range of 760 nm – 900 nm, which is not as narrow as the NIR bandwidth range of 700 nm – 900 nm on the Landsat-5 MSS. According to Jensen

2007, the precision of bandwidth sensitivity is best analyzed by a typical Gaussian shape and by determining the Full Width at Half Maximum (FWHM).

1.2.3 Radiometric Resolution

Radiometric resolution, referred to as the quantization level, is the remote sensing detector's sensitivity to differences in signal strength as it records the radiant flux reflected, emitted, or back-scattered from the imaged object (Jensen 2007). An analog-to-digital conversion occurs onboard a remote sensing platform that quantizes the collected data into what is known as the radiometric resolution, which defines the range for pixel values within a certain image. For an example, 8-bit unsigned data have a possible range between 0-255; a total of 256 possible integers to represent each pixel value within an image. The typical quantization levels in Table 1.1 represent higher and lower radiometric resolutions. A remote sensing platform with a higher radiometric resolution will image in a larger domain of pixel values and provides a higher probability of image accuracy.

Table 1.1 Common Radiometric Resolutions in Remote Sensing

	Radiometric Resolutions				
Quantization Levels	6-bit	8-bit	10-bit	12-bit	16-bit
Value Ranges	0 - 63	0 - 255	0 - 1,023	0 - 4,095	0 - 65,535

1.2.4 Temporal Resolution

Temporal resolution is defined by the frequency at which a remote sensing platform can collect data of a certain object. Higher temporal resolution refers to the

ability of a remote sensing platform to repetitively collect data of an object more often than a lower temporal resolution platform. Temporal resolution greatly vary depending on the aerial imaging platform; however, orbiting satellites such as Landsat-7 have a fixed temporal resolution, in which it images a certain area on the Earth every 16 days.

1.3 Landsat Program Overview

1.3.1 Historical Relevance

The Landsat program is the longest running satellite mission providing imagery for Earth, which has immensely impacted many fields within geosciences. Initiated in 1972, the Landsat program has launched eight and maintained seven versions of satellites (Knight and Kvaran 2014). Despite a failed mission in Landsat-6, in which an orbital destination was never reached, the Landsat program exemplifies an impressive history in remote sensing.

Landsat started as an experimental satellite initially deemed the Earth Resources Technology Satellite (ERTS) program by the National Aeronautics & Space Administration (NASA) in 1967 with the primary mission of collecting Earth resources data. The first of the series, ERTS-1, launched on July 23rd, 1972, and aimed to test the performance of collecting Earth data from an unmanned satellite (Jensen 2007). After successful ERTS-1 operations and the design of ERTS-B, NASA renamed the program 'Landsat' in January of 1975 to avoid confusion with the 'Seasat' satellite scheduled to launch in 1978. Subsequently, ERTS-1 and ERTS-B became known as Landsat-1 and Landsat-2, respectively.

The original Landsat technology gained a reputation of successful data collection with its Multispectral Scanner (MSS) sensor. The MSS was installed on Landsats 1

through 3, and also joined with the Thematic Mapper (TM) sensor introduced on Landsat 4 and 5, which improved the spatial, spectral, temporal, and radiometric resolution relative to the MSS. Landsat-7 introduced the Enhanced Thematic Mapper Plus (ETM^+) in 1999. The ETM^+ did not increase any of said resolutions relative to the TM; however, a milestone in the Landsat program was reached with the release of the Operational Land Imager (OLI) and Thermal Infrared Sensor (TIRS) installed on Landsat-8. Launched in February 2013 under the label, 'Landsat Data Continuity Mission (LDCM)', Landsat-8 operates the OLI and TIRS simultaneously, but independently (Reuter et al. 2015).

1.3.2 Remote Sensing Resolutions

The original MSS performed with a spatial resolution of 79 m for bands 4 through 7, a spectral resolution represented by bands 4 through 7, and 8 (band 8 only found on Landsat-3), a temporal resolution of 18 days (Landsats 1-3) and 16 days (Landsats 4 and 5), and a radiometric resolution of 6-bit (0-63) (Jensen 2007). Also installed on Landsat 4 and 5 was the TM sensor with an improved spatial resolution of 30 m, spectral resolution of bands 1-7, temporal resolution of 16 days, and a radiometric resolution of 8-bit. Landsat-7's ETM^+ and Landsat-8's OLI also featured a spatial resolution of 30 m and temporal resolution of 16 days. However, the ETM^+ and OLI differs in spectral and radiometric resolutions. The ETM^+ operates with a spectral resolution imaging in eight bands and the OLI imaging in nine bands. Additionally, Landsat-8 includes the TIRS that thermally images with two bands at a spatial resolution of 120 m. Table 1.2 describes the sensor specifications for Landsat 4 – 8.

1.3.3 Applications

Landsat-8 was designed and launched with the intention of maintaining the continuous imaging of the previous Landsat-7 (Roy et al. 2014), as well as to distribute multispectral imagery at a scale to monitor natural and human-induced changes over time (Reuter et al. 2015). The OLI and TIRS operating onboard Landsat-8 extends the Landsat program by providing global imagery to the USGS Earth Resources Observation and Science Center (EROS) and the National Satellite Land Remote Sensing Data Archive (NSLRSDA) (Reuter et al. 2015).

The Landsat program has consistently collected large-scale imagery of land and water over time. An invaluable spectral range that Landsat remote senses in is the Near-Infrared (NIR) wavelength. Government agencies such as the U.S. Department of Agriculture (USDA) often use Landsat imagery as an effective method of monitoring large crop farms. For example, the USDA has implemented the Cropland Data Layer (CDL), which uses 30 m spatial resolution to annually account for over 100 land cover and crop type classes for the contiguous U.S. (Roy et al. 2014). Due to the improved radiometric resolution of the OLI, the USDA has integrated Landsat-8 data into the CDL generation. However, its low temporal and spatial resolution creates a difficult task when attempting to collect data in more localized parameters; hence, the UAS integration initiative set forth by the Boulder, CO workshop described in Section 1.1.

Table 1.2 Specifications of Landsat Sensors

	Landsat 4 and 5 (MSS)		Landsat 7 (ETM^+)		Landsat 8 (OLI/TIRS)	
Spectral Resolution	Band	Wavelength Ranges (nm)	Band	Wavelength Ranges (nm)	Band	Wavelength Ranges (nm)
	1	500 – 600	1	450 – 520	1	430 – 450
	2	600 – 700	2	520 – 600	2	450 – 510
	3	700 – 800	3	630 – 690	3	530 – 590
	4	800 – 1100	4	760 – 900	4	640 – 670
			5	1550 – 1750	5	850 – 880
			6	1040 – 1250	6	1570 – 1650
			7	2080 – 2350	7	2110 – 2290
					8	500 – 680
					9	1360 – 1380
					10	1060 – 1119
					11	1150 – 1251
Spatial Resolution (m)	79 x 79		30 x 30 60 x 60 (Band 6)		30 x 30 (Bands 1-6,7,9) 15 x 15 (Band 8) 100 x 100 (Bands 10,11)	
Radiometric Resolution	6 Bit (0 – 63)		8 Bit (0 – 255)		16 Bit (0 – 65,535)	
Temporal Resolution	16 Days		16 Days		16 Days	
Altitude (m)	9.19×10^5		7.05×10^5		7.05×10^5	
Swath (m)	1.85×10^5		1.85×10^5		1.85×10^5	

(Jensen 2007 and Roy et al. 2014)

1.4 Unmanned Aerial Systems

1.4.1 Definitions and Features

The terms Unmanned Aerial Vehicle (UAV), Unmanned Aircraft (UA), and Unmanned Aerial System (UAS) are widely used as synonymous representations; however, one would benefit from understanding the difference in components involved with each technology. A UAV is just that, an aerial vehicle that is flown without an on-board pilot. Similar to a UA, the UAV is referring to the aircraft itself. A UAS includes a longer list of components such as: the UA/UAV (platform), a remote pilot or operator, a

Ground Control Station (GCS) where the pilot operates the aircraft, a communication unit that transfers information from the GCS and UA/UAV, the payload and/or payload operator used for remotely sensed data collection, and spotters that monitor the flight and any hazards that may come near the flight path (Whitehead et al. 2014, Cress et al. 2015).

The GCS can be considered the mission operation center of the UAS. This is the location where all components of the UAS are linked together. The pilot operates the aircraft from the GCS with the visual assistance of spotters that warn of any flightpath hazards. The remote sensing equipment installed on UASs for operational data collection missions is referred to as the payload. Payloads vary depending on mission requirements and desired data sought. The communication unit allows the pilot to control the aircraft from the GCS and simultaneously provides a link to transmit payload data such as live video images, compass headings, and location information (Cress et al. 2015).

UASs are designed with many various UAV shapes and sizes; however, according to Hugenholtz (2012) and Whitehead et al. (2014), there are only two main types of UAS configurations: rotary wing and fixed wing (helicopter and airplane, respectively). Additionally, the two configurations are separated into five UAV classifications: Micro (<0.9 kg), Mini (0.9-13.6 kg), Tactical (13.6-454.5 kg), Medium Altitude Long Endurance (454.5-13,636.4 kg), and High Altitude Long Endurance (>13,636.4 kg). Adding to this list of classifications, Watts et al. (2012) identifies: Nano Air Vehicles (NAVs), Vertical Take-off & Landing (VTOL), Low Altitude, Short-Endurance (LASE), and Long Altitude, Long-Endurance (LALE).

Another UAV classification of UAS technology will be made available to fly in the National Air Space (NAS), which is deemed by the Federal Aviation Administration

(FAA) as “small UAS” (sUAS) (Hugenholtz 2012). In order to define a sUAS per FAA, a thorough explanation is needed for a “small unmanned aircraft” itself. The FAA states that Public Law 112-95 defines a “small unmanned aircraft” as weighing less than 24.9 kg (Huerta and Foxx 2015); however, the FAA proposes to update the stated definition by limiting the total takeoff weight of the small unmanned aircraft to less than 24.9 kg to reduce the damage threat. Despite the FAA classifying platforms weighing less than 24.9 kg as sUAS, the components required for operation are the same (Cress et al. 2014).

An important advancement in sUAS technology is the development of an autopilot option that includes several integrated components: GPS receiver, micro-inertial navigation system, microprocessor, and a flight data recorder. The GPS receiver measures the absolute aircraft position and airspeed while the micro-inertial navigation system measures the aircraft attitude. The microprocessor provides input to aircraft flight controls and the flight data recorder logs the position and attitude parameters for each image (Hugenholtz, 2012).

1.4.2 Historical Relevance

UAS is a new term relative to the history of UAVs/UAs. Contrary to popular belief, UAVs/UAs have been around for many years; in fact, decades before the use of satellite technology. Veritably, the first UAV was manufactured by the American Lawrence and Sperry (ALS) in 1916, which they initially coined as, “Aviation Torpedo” (Gupta et al. 2013). This was also thought to be the beginning of ‘attitude control’, referring to the automatic steering of an aircraft. According to Gupta et al. (2013), the “Aviation Torpedo” developed by ALS flew in excess of 48 km.

Decades following the first UAV, the military adopted its technology in the late 1950s. Full scale research and development was initiated by real-world application opportunities in the Vietnam and Cold wars, extending into the 1970s with a UAV called "Fire Bee." The size and cost of the UAV technology was reduced post-Vietnam War, as a result of the US and Israel's interest. Subsequently, these newer UAVs were powered by motorcycle and snow-mobile engines that transmitted images to the operator's location from an onboard video camera. This idea was considered the prototype of modern UAV technology (Gupta et al. 2013).

After an impressively long conception of the UAV, popularity of the technology remained in the interests of military operations throughout the 1900s. The use of the popular General Atomics MQ-1 Predator in the first Gulf war is an excellent example of how the world perceived the relevance of unmanned flight. Military UA operations have continued to grow over the last 20 years with the use of over 20 different UASs flying overseas missions from four branches: Air Force, Navy, Marine Corps, and Army. Moreover, the U.S. military has increased total UAS flight hours from less than 50 thousand in the year 2000 to over 550 thousand in 2010 (Spriesterbach et al. 2013).

1.4.3 Applications

Military UAV operations in the Gulf War initialized the logic of practical use that spread beyond the US Armed Forces. After over a decade of research and development, various U.S. government agencies, such as the Department of the Interior (DOI) U.S. Geological Survey (USGS), began experimenting with UAS technology. A popular mission planned by the DOI occurred in 2004 during a volcanic event on Mount Saint Helens, Washington. The successful mission highlighted the benefits of using UAS

technology as a cost-effective remote sensing method for scientific, environmental, and land management applications (Cress et al. 2015). Following the successful demonstration of UAS potential at Mount Saint Helens, the USGS began adopting UAS technology. In 2005, a USGS Land Remote Sensing Program concluded the following after investigating UAS technology: UAS military use was increasing exponentially, many civil agencies were implementing UAS program offices, U.S. universities were creating UAS degree programs, and there was a rapid increase in UAS vendors (Cress et al. 2015).

UAS technology began to spread beyond the U.S. in the 2000s at the International Society for Photogrammetry and Remote Sensing (ISPRS) congress in Istanbul. The congress passed Resolution I.1 in 2004, noting: UAVs provide a new controllable platform for remote data acquisition, the maneuverability of UAVs allow remote data acquisition in dangerous environments that are inaccessible to direct examination, and UAVs provide a cost-effective option with more rapid data acquisition than manned aircraft (Everaerts, 2008). Wide ranges of applications are being considered for UAS technology such as: military intelligence, surveillance and reconnaissance (ISR), border security, attack and strike, target identification and designation, environmental, agricultural, aerial mapping and meteorology (Gupta et al. 2013). The vast amount of payloads that UASs can carry are only increasing its potential in such applications.

1.5 Research Objective

Suborbital aerial imaging is becoming a more liable method of collecting data in the remote sensing field; whereas satellite imaging has a reliable history of collecting data. Various types of UAS platforms are increasingly operated by government agencies,

universities, and research teams due to its cost-efficient and highly-modifiable characteristics; however, the Landsat program has a long period of reliable data collection for observing Earth, which includes land surface classifications. UAS platforms are designed to collect data over a relatively concentrated area, opposed to larger coverage of Landsat-8 OLI imagery. As a result, research is needed to quantitatively and qualitatively compare data from the two platforms to define the abilities associated with using UAS imagery along with, or even in place of, existing Landsat data.

The objective of this research is to compare imagery from two different remote sensing platforms: Landsat-8 and UAS NB3. The purpose of the imagery comparison is to test an upward trending remote sensing method versus reliable satellite technology. Each platform will be analyzed in four remote sensing resolutions: spatial, spectral, radiometric, and temporal. The imagery comparisons will be tested by detecting land and water features within the Lower Pearl River Basin, where inundation caused by Hurricane Isaac challenged National Weather Service (NWS) River Forecast Centers (RFCs). This research will evaluate satellite imagery versus UAS imagery with the analysis of land-water masks and statistical comparisons using the near-infrared (NIR) spectral band on-board Landsat-8 and NB3 platforms. Upon the completion of land-water masks and statistical comparisons of Landsat-8 imagery and corresponding NB3 imagery, a thorough qualitative and quantitative analysis of each remote sensing resolution will be presented and discussed.

CHAPTER II

METHODS AND MATERIALS

2.1 Remote Sensing Platforms

2.1.1 UAS

This research employed a sUAS with a 6.8 kg fixed-wing UA/UAV that measured 1.8 m in length with a wing span of 2.7 m and carried a Nova Block 3 (NB3) payload. The NB3 payload supported a Canon EOS Rebel SL1 with a Kodak Wratten deep yellow #12 longpass gel filter with a spectral resolution of three bands (red, green, and blue). The longpass gel filter was designed to attenuate lower spectral responses of less than 500 nm (blue band), and transmit at an optimal spectral response between 792-873 nm (band-3) to simulate that of a NIR band. The Canon EOS Rebel SL1 imaged from an along-track 40.9° Field of View (FOV). The spatial resolution of the Canon EOS Rebel SL1 was ≈0.05 m from 243 m Above Ground Level (AGL) with an 8-bit unsigned radiometric resolution. The specifications of the NB3 Canon EOS Rebel SL1 are compared to Landsat-8 OLI in Table 2.1.

The UAS employed for this research was maintained and operated by Altavian Inc. in conjunction with Mississippi State University (MSU) and the Northern Gulf Institute (NGI) with a temporal return of two months. Due to the temporal resolution of Landsat-8 and the research schedule of the UAS mission, the Landsat-8 data did not occur over the same time period as the NB3 data. As such, the NB3 data used in this

research were selected with the intention of finding the closest temporal match to reliable Landsat-8 data, which is compared in Table 2.2 and Table 2.3.

Table 2.1 Specifications of Landsat-8 OLI and NB3 Canon EOS Rebel SL1 Imagery

	Spatial Resolution	Spectral Resolution	Temporal Resolution	Radiometric Resolution	Coverage Area	Sensor Type
Landsat-8 OLI	30 m Band 5	850 - 885 nm Band-5	16-Day Return	16 bit 0 - 65,535	1.85×10^5 m x 1.80×10^5 m	Operational Land Imager
NB3 Canon EOS	≈0.05 m Band 3	792 - 873 nm Band-3	Mission Variable	8 bit 0 - 255	272 m x 182 m	Canon EOS Rebel SL1

2.1.2 Landsat-8

Landsat-8 platform was equipped with an OLI payload that integrates a linear array pushbroom sensor technology. The pushbroom sensor onboard Landsat-8 simultaneously senses an entire row with detectors per channel that sweeps in the along-track direction by spacecraft motion. Sensing an entire row simultaneously allows the OLI to receive stronger signals and improve signal-to-noise performance (Li et al. 2013). Additionally, an Image Assessment System (IAS) was developed to operationally monitor, characterize, and update the OLI (Reuter et al. 2015).

The spectral resolution of the OLI includes bands 1-9 are described in Table 1.2. Band-5 on the OLI was calibrated as NIR, which had an optimal spectral response between 850-880 nm with a spatial resolution of 30 m at an orbiting altitude of 7.05×10^5 m above the Earth's surface. Each Landsat-8 OLI image had a 16-bit unsigned radiometric resolution and a temporal resolution of 16 days, in which the localized

research parameter in the LPRB was remotely sensed from a sun-synchronous near-polar orbit.

Table 2.2 Full extent for NB3 Canon EOS Rebel SL1 and Landsat-8 OLI

Platform	Date	Δ Days	Pixel Values	Threshold Values
NB3 Canon EOS	3/19/2015	8	42 - 255	157
Landsat-8 OLI	3/27/2015		01 – 255	118
NB3 Canon EOS	3/16/2015	11	67 - 255	163
Landsat-8 OLI	3/27/2015		01 – 167	96
NB-3 Canon EOS	12/18/2014	17	75 - 255	186
Landsat-8 OLI	1/6/2015		04 – 187	93
NB-3 Canon EOS	12/16/2014	21	01 - 255	128
Landsat-8 OLI	1/6/2014		23 - 252	75

Landsat-8 OLI data are managed and archived by the USGS Earth Resources Observation Systems (EROS) Data Center. All Landsat-8 OLI global and synoptic data are electronically distributed for public use as level-1 radiometrically calibrated and orthorectified images in the standard Worldwide Reference System 2 (WRS2) grid (Reuter et al. 2015). Landsat-8 OLI data were made available by the USGS as a no-cost download through three platforms; EarthExplorer, Global Visualization Viewer (GloVis), and LandsatLook Viewer.

2.2 Digital Image Processing

Collecting remotely sensed data must be transformed into information that can be interpreted and analyzed. Remotely sensed platforms convert the analog data to digital values that are organized and stored in a matrix. The digital values of the collected data are stored in columns and rows, which collectively create a pixel. A pixel is a two-dimensional representation of the smallest nondivisible element of a digital image

(Jensen 2007). After remotely sensed data is collected and digitally converted, the stored pixels within the matrix are each assigned a Brightness Value (BV). These BVs are bounded by the calibrated quantization level of the remotely sensed platform. The NB3 Canon EOS Rebel SL1 had an 8-bit unsigned radiometric resolution quantized to an output BV range of 0-255. The Landsat-8 OLI data was digitally processed and quantized in 16-bit radiometric resolution with an output range of 0-65,535. Several matrices are stored in multispectral remote sensing systems; however, each band has its own matrix with unique BVs.

An equal comparison of the Landsat-8 OLI and NB3 Canon EOS Rebel SL1 required both images to share the same spatial extent and quantization levels. The higher radiometric resolution of the OLI 16-bit was downsampled to an 8-bit quantization level using the nearest neighbor method. The spatial extent of the comparing Landsat-8 OLI and NB3 Canon EOS Rebel SL1 imagery was matched at two different scales: full extent of Canon EOS Rebel SL1 and an area of interest (AOI) of $\approx 3.00 \times 10^5$ m^2. Both scales were used in comparing the two remote sensing platforms and are shown in Figure 2.1.

2.3 Comparisons

2.3.1 Land-Water Masks

A remote sensing detector measures the total amount of radiance as a function of the electromagnetic energy from four sources: atmospheric scattering, water-surface radiance, subsurface volumetric radiance, and bottom of the water radiance (Jensen 2007). The total amount of radiance measured from a remotely sensed platform over an area of pure water is the sum of all four sources as explained in Equation 2.1:

$$L_t = L_b + L_p + L_s + L_v \quad (2.1)$$

where L_b is the measured radiance from the solar and atmospheric irradiance that penetrates the surface of the water, reaches the bottom and propagates upward through the air-water boundary. L_p is the source of radiance that never reaches the surface of the water, but is scattered and measured as atmospheric noise. L_s is the solar and atmospheric irradiance that barely penetrates the surface of the water before reflecting back towards the platform sensor. L_v is measured from solar and atmospheric irradiance that penetrates the water, interacts with the organics and inorganics within the water, then reflects back through the air-water boundary without reaching the bottom of the water body.

Measuring the total radiance with each platform in this research was presented with the creation of land-water masks. Land-water masks are a widely used technique of visualizing classifications from data collected by a remote sensing platform. The creation of land-water masks in this research adopted the density slicing method to classify between land and water in the localized research parameter (Figure 1.1) for each platform. Density slicing was the preferred method in this research, in which a single spectral band was separated from both platform's multispectral digitally processed collection of data. This research aimed to density slice the NIR wavelength from the Landsat-8 OLI and NB3 Canon EOS Rebel SL1 (band 5 and band 3, respectively).

The NIR band is the optimal wavelength for classifying between land and water due to its absorptivity and reflectivity characteristics of solar and atmospheric irradiance. According to Jensen 2007, water features in the NIR and mid-NIR wavelengths (740 – 2500 nm) are relatively dark-colored in imagery because they absorb almost all of the incident radiance, opposed to the relatively high radiance reflectance of vegetation. The collected data in the NIR wavelength, shown in Figure 2.1, returns BVs that represent the

total measured radiance that was absorbed and reflected by the water and land, respectively. The density slicing method considers the BVs as a representation of the measured object's density values, such that lower density values will result in darker-colored pixels (water) within the subject imagery. Conversely, the higher measured density values from reflected radiance in vegetation will be represented as brighter-colored pixels (land).

The method used in this research to classify between land and water in the density sliced data for each platform is referred to as 'natural breaks' with Jenks Optimization. The original natural breaks method required the cartographer to analyze the data distribution and subjectively decide where the appropriate class breaks should exist. This method's subjectivity was reduced by the development of the Jenks Optimization approach, and is now considered one of the major techniques for class delineation. Jenks Optimization identifies the breaks in the attribute value range by minimizing the sum of the variance within each of the classes, which suggests a maximization of homogeneity for each classification (Murray et al. 2000). The threshold values used for the creation of land-water masks in this research are described in Table 2.2 (full extent) and Table 2.3 (AOI).

The threshold values for each land-water mask were based on natural breaks with Jenks Optimization for two classes: land and water. Each image were expected to have different threshold values, thus, a natural break with Jenks Optimization was determined for each image. The two scales at which land-water masks were compared in this research were: the full extent of the Canon EOS Rebel SL1 and AOI $\approx 3.00 \times 10^5$ m^2; which are described in Table 2.2 and Table 2.3, respectively.

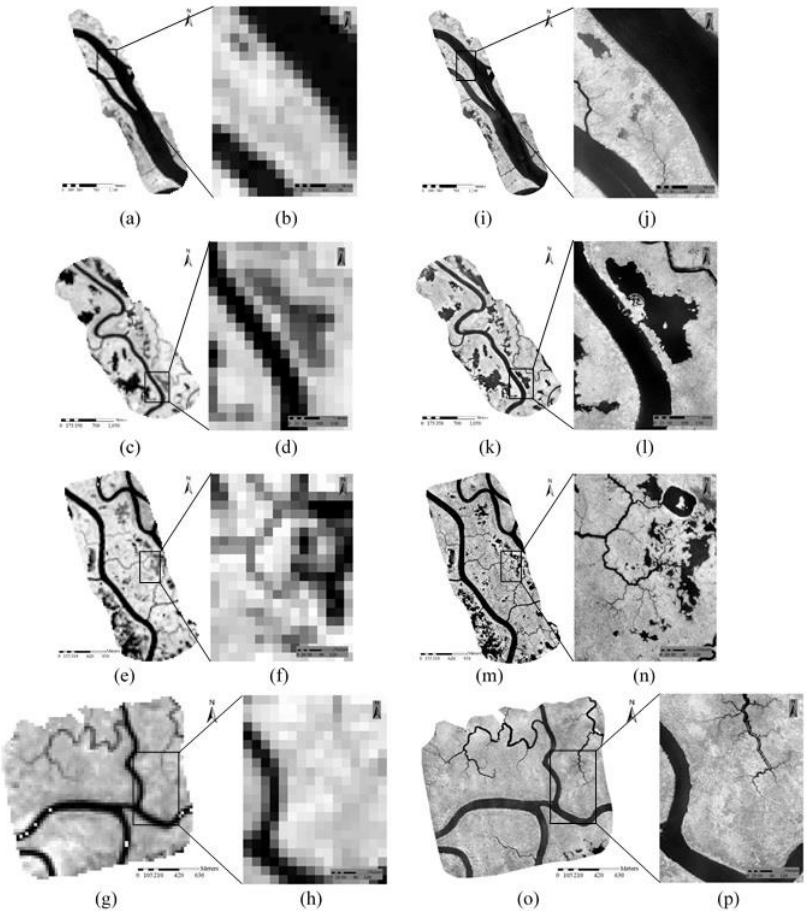

Figure 2.1 Landsat-8 and NB3 NIR Imagery

Full extent and AOI NIR imagery of 8-bit Landsat-8 vs. NB3: (a,b) Jan. 06th OLI vs. (i,j) Dec. 16th Canon EOS, (c,d) Jan. 06th OLI vs. (k,l) Dec. 18th Canon EOS, (e,f) Mar. 27th OLI vs. (m,n) Mar. 16th Canon EOS, (g,h) Mar. 27th OLI vs. (o,p) Mar. 19th Canon EOS. Note: Areas of no data are found in (g) Mar. 27th OLI.

Table 2.3 AOI extent for NB3 Canon EOS Rebel SL1 and Landsat-8 OLI

Platform	Date	Δ Days	Pixel Values	Threshold Values
NB3 Canon EOS	3/19/2015	8	82 - 222	150
Landsat-8 OLI	3/27/2015		04 - 231	111
NB3 Canon EOS	3/16/2015	11	99 - 227	162
Landsat-8 OLI	3/27/2015		85 - 158	130
NB3 Canon EOS	12/18/2014	17	123 - 253	181
Landsat-8 OLI	1/6/2015		26 - 163	98
NB3 Canon EOS	12/16/2014	21	48 - 236	126
Landsat-8 OLI	1/6/2014		24 - 157	76

2.3.2 Statistical Comparisons

Statistically comparing imagery in this research was based on the exact AOI spatial extents used for the land-water masks. A major difference was adding a NB3 Canon EOS Rebel SL1 image that matched the 30 m spatial resolution of Landsat-8 OLI. This downsample of spatial resolution for the Canon EOS Rebel SL1 from ≈0.05 m to 30 m was to ensure an unbiased statistical comparison with the exact spatial alignment, shown in Figure 2.2. Resampling both images to match spatial and radiometric resolutions was completed before converting the imagery from GeoTIFF to ASCII dataset format.

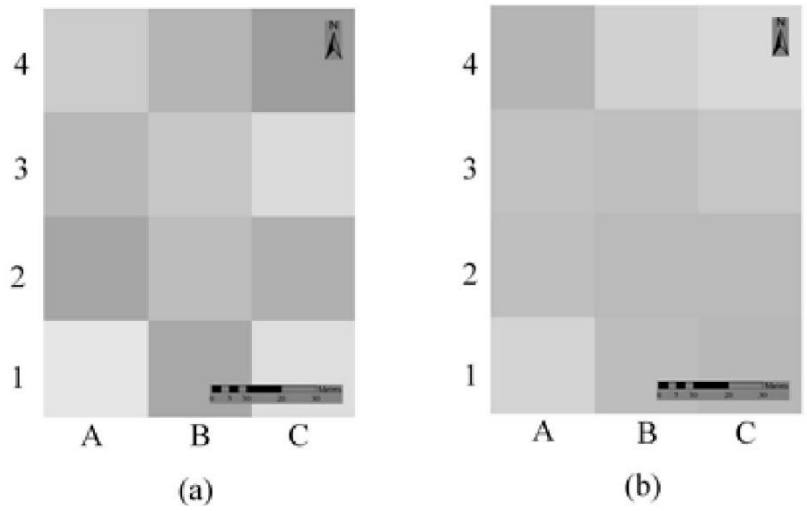

Figure 2.2 Landsat-8 and NB3 NIR Grid

30 m NIR imagery grid of (a) January 6th Landsat-8 OLI vs. (b) December 16th NB3 Canon EOS Rebel SL1

The resulting ASCII file was processed into a binary vector dataset and classified as either water (0) or land (1) with threshold values determined by the natural breaks

method with Jenks Optimization. Calculating the water and land percentages of each image was completed using Equation 2.2 and Equation 2.3:

$$\mathrm{Wp} = (\sum_{i=0}^{n} Wc / \sum_{i=0}^{n} Tc) x100 \tag{2.2}$$

$$\mathrm{Lp} = (\sum_{i=0}^{n} Lc / \sum_{i=0}^{n} Tc) x100 \tag{2.3}$$

where the percentage of water pixels and land pixels in the subject image are represented as *Wp* and *Lp*, respectively. *Wc* is the total number of water pixels in the subject image, *Lc* is the total number of land pixels in the subject image, and *Tc* is the total number of pixels in the subject image.

To ensure the spatial alignment of each NB3 image with its corresponding Landsat-8 image, an additional statistic was accomplished to compare pixels in space. Each pixel was classified as either water (0) or land (1) as previously described in the statistical comparison. Figure 2.2 shows a gridded example of how corresponding images were compared in space. The A1 - C4 pixels between Figure 2.2a and 2.2b were spatially matched by classifying each pixel value as land or water, subsequently calculating the matched percentage of the corresponding pixels.

CHAPTER III

RESULTS

3.1 Spatial Resolution

3.1.1 Land-Water Masks

With respect to spatial resolution, the land-water masks for the full-extent scale between the NB3 Canon EOS Rebel SL1 and Landsat-8 OLI imagery slightly differ as far as suggesting water versus land. Figure 3.1 presents the overall land-water mask comparisons of each NB3 Canon EOS Rebel SL1 and corresponding Landsat-8 OLI imagery at full-extent. Figure 3.2 shows the AOI extent comparison between the OLI and Canon EOS Rebel SL1. The coarser resolution of the Landsat-8 OLI creates relatively rigid shorelines and areas of water within the marsh terrain, opposed to the NB3 Canon EOS Rebel SL1 higher resolution showing more distinct shorelines and suggested areas of water.

The spatial resolution aspect of each platform yielded major differences in comparing land-water masks at the AOI scale. All four NB3 Canon EOS Rebel SL1 land-water masks at the AOI extent have areas that suggest water that are not found in the corresponding Landsat-8 OLI imagery. Conversely, there is a low frequency of occurrence where the Landsat-8 OLI at the smaller AOI suggests water in areas where the NB3 Canon EOS Rebel SL1 suggests land. The coarser resolution of the Landsat-8 OLI

is evident in Figure 3.2 with respect to the AOI extent, which has a more noticeable disagreement between the two platforms.

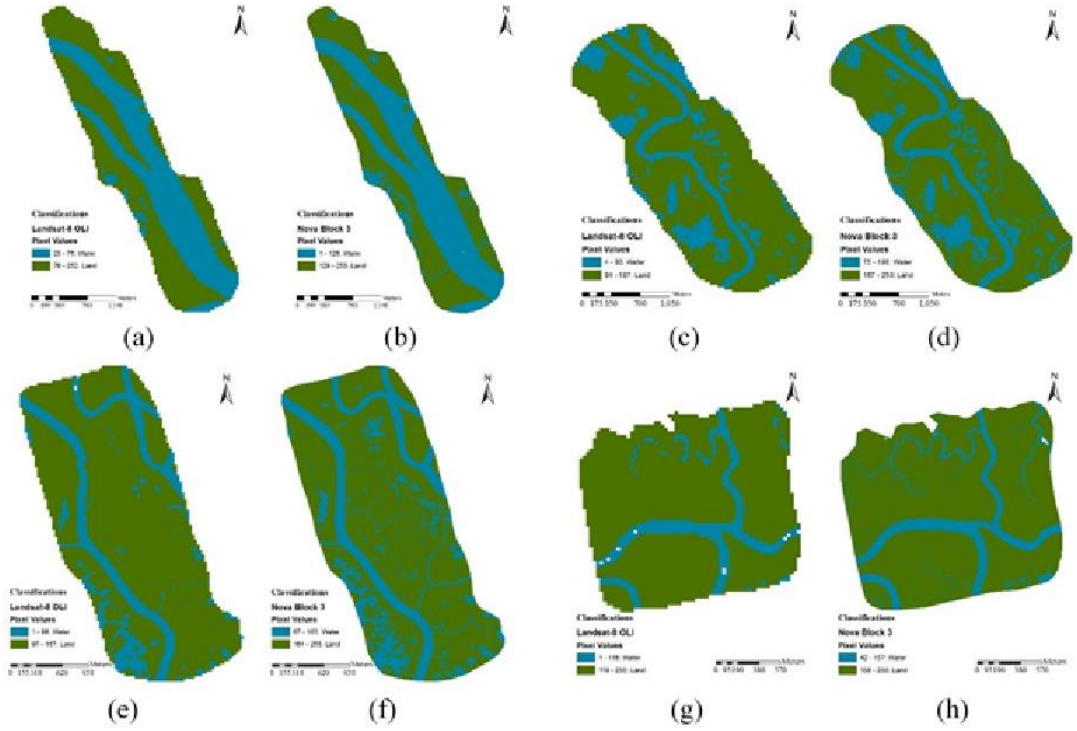

Figure 3.1 Land-Water Mask Comparisons

Comparison of the full extent land-water masks of Landsat-8 vs. NB3: (a) Jan. 06th OLI vs. (b) Dec. 16th Canon EOS, (c) Jan. 06th OLI vs. (d) Dec. 18th Canon EOS, (e) Mar. 27th OLI vs. (f) Mar. 16th Canon EOS, (g) Mar. 27th OLI vs. (h) Mar. 19th Canon EOS. Note: Areas of no data are found in (g) Mar. 27th OLI and (h) Mar. 19th Canon EOS.

The LPR as well as a primary and secondary tributary are evident in the NB3 land-water mask (Figure 3.2b); however, the corresponding Landsat-8 mask (Figure 3.2d) fails to suggest the secondary tributary and only senses the large primary tributary and LPR. A similar disagreement between the NB3 and Landsat-8 land-water masks is shown in Figures 6n and 6p, respectively, where the NB3 suggests a substantial stream with

associated branches. An interesting difference in land-water masks is noted in Figures 6f and 6h, where both masks classify the large area on the eastern section of the LPR as water, but only the NB3 mask has a suggested narrow entry point location.

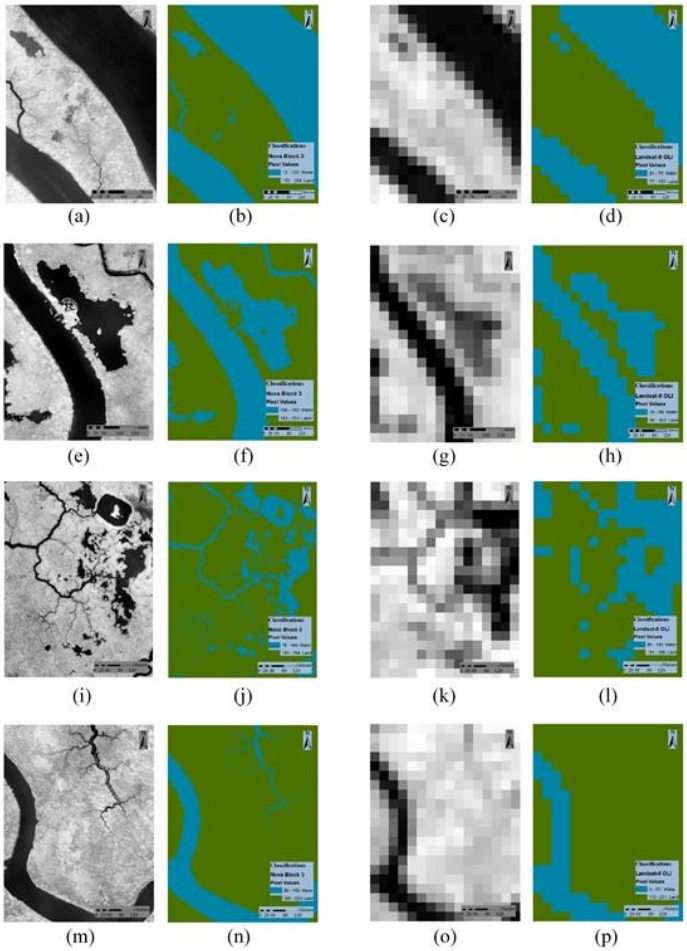

Figure 3.2 Landsat-8 and NB3 NIR and Land-Water Masks

AOI NB3 and Landsat-8: (a) Dec. 16th Canon EOS NIR and (b) mask vs. (c) Jan. 06th OLI NIR and (d) mask, (e) Dec. 18th Canon EOS NIR and (f) mask vs. (g) Jan. 06th NIR and (h) mask, (i) Mar. 16th Canon EOS NIR and (j) mask vs. (k) Mar. 27th OLI NIR and (l) mask, (m) Mar. 19th Canon EOS NIR and (n) mask vs. (o) Mar. 27th NIR and (p) mask.

3.1.2 Statistical Comparisons

Overall, the 30 m spatial resolution AOI comparisons had an average difference of 1.77% pixel values of water and land, as shown in Table 3.1. The largest classification difference in the comparing imagery was 20.41% between the March 16th NB3 Canon EOS Rebel SL1 and March 27th Landsat-8 OLI. Additionally, the comparing histogram distribution between March 16th NB3 Canon EOS Rebel SL1 and March 27th Landsat-8 OLI has the largest difference between any of the other AOI comparisons, shown in Table 3.1.

Table 3.1 Statistical Comparison Results

Remote Sensing Platform	Water Pixels (Wc)	Land Pixels (Lc)	Total Pixels (Tc)	Water Percentage (Wp)	Land Percentage (Lp)	Water Percentage (Avg)	Land Percentage (Avg)
Landsat-8 OLI						**32.71%**	**67.29%**
19-Mar	25	215	240	10.42%	89.58%		
16-Mar	95	145	240	39.58%	60.42%		
18-Dec	86	154	240	35.83%	64.17%		
16-Dec	108	132	240	45.00%	55.00%		
NB3 Canon EOS Rebel						**30.94%**	**69.06%**
19-Mar	28	212	240	11.67%	88.33%		
16-Mar	46	194	240	19.17%	80.83%		
18-Dec	104	136	240	43.33%	56.67%		
16-Dec	119	121	240	49.58%	50.42%		

Three of the four comparing images had over an 87% spatial match with respect to land and water pixels. Table 3.2 shows the results of the statistical alignment between each Landsat-8 and NB3 image. The anomaly of the four spatial statistic is found in the March 16th comparison; whereas, a 67.92% match between land and water pixels

between the two platforms. This anomaly is 19.58% lower than the next lowest alignment statistic of 87.50% found in the December 18th comparison.

Table 3.2 Spatial Alignment of Landsat-8 OLI and NB3 Canon EOS Rebel SL1

Date	Match	Non-Match	Total Pixels	Percent Match
19-Mar	231	9	240	96.25%
16-Mar	163	77	240	67.92%
18-Dec	210	30	240	87.50%
16-Dec	223	17	240	92.92%

3.2 Spectral Resolution

The spectral responses of each platform sensor are shown in Figure 3.3, which include the Canon EOS Rebel SL1 with and without the Kodak Wratten deep yellow #12 longpass gel filter. As displayed in the Figure 3.3, the longpass filter attenuates band 3 (blue band) in wavelengths less than 500 nm. This attenuation allows band 3 to measure the radiance reflected in the optimal range of the NIR wavelength (792 – 873 nm). Landsat-8 OLI has a more narrow optimal NIR wavelength range (850 – 880 nm).

A comparison of the original 16-bit Landsat-8 OLI to the 8-bit NB3 EOS Rebel SL1 with respect to their spectral responses are shown in Figure 3.4. The central wavelengths of green, red, and NIR for the Canon EOS Rebel SL1 were 540 nm, 610 nm, and 820 nm, respectively. Landsat-8 OLI had central wavelengths for green, red, and NIR of 561 nm, 655 nm, and 865 nm, respectively. As mentioned in section 2.3.1, the BVs are indicative of the absorptivity and reflectivity characteristics at a measured wavelength.

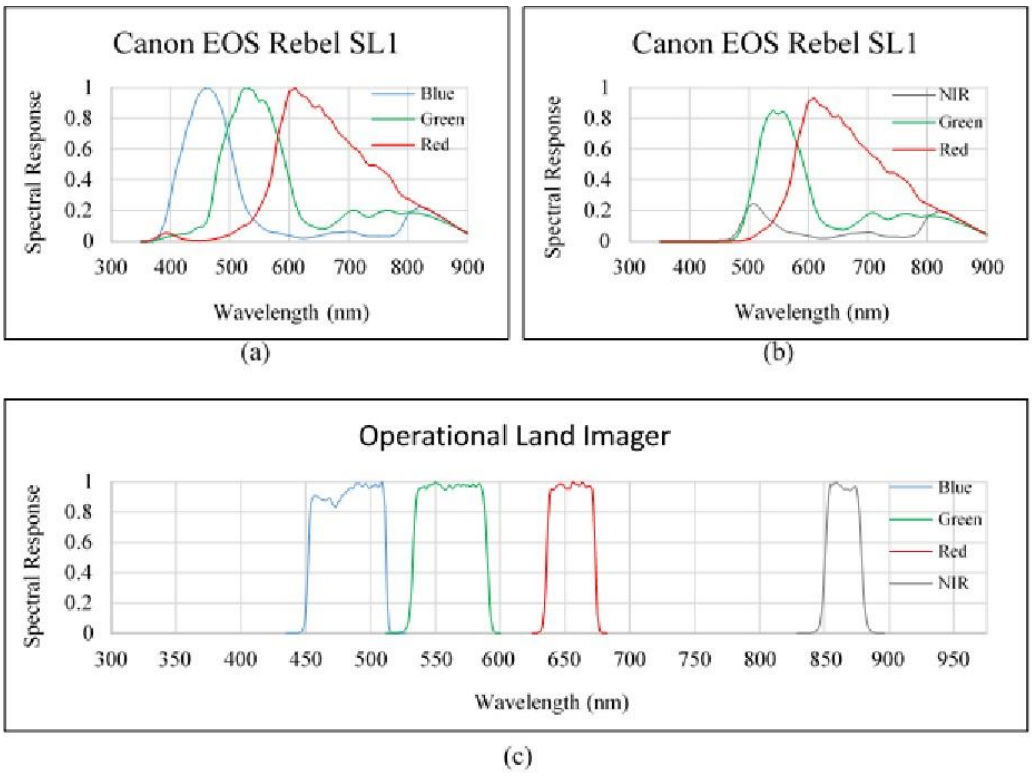

Figure 3.3 Landsat-8 and NB3 Spectral Resolution

(a) Spectral comparison between the original unfiltered Canon EOS, (b) Canon EOS with the Kodak Wratten #12 deep yellow NIR gel filter, (c) and Landsat-8 OLI.

Both sensors show a similar overall spectral response to areas of vegetation and water with respect to wavelengths and BVs. The difference between the OLI and Canon EOS Rebel SL1 around the 540 nm – 561 nm wavelengths shows a wider range of measured BVs due to the different calibrated central wavelengths between NB3 Canon EOS Rebel SL1 and Landsat-8 OLI. The gradual decline in BVs shown in Figures 8a and 8c, suggests more absorption of water areas measured at higher wavelengths. Figures 8b and 8d shows the spectral response of vegetation; which is indicative of the higher reflectivity of land areas in the localized research parameter of the LPRB.

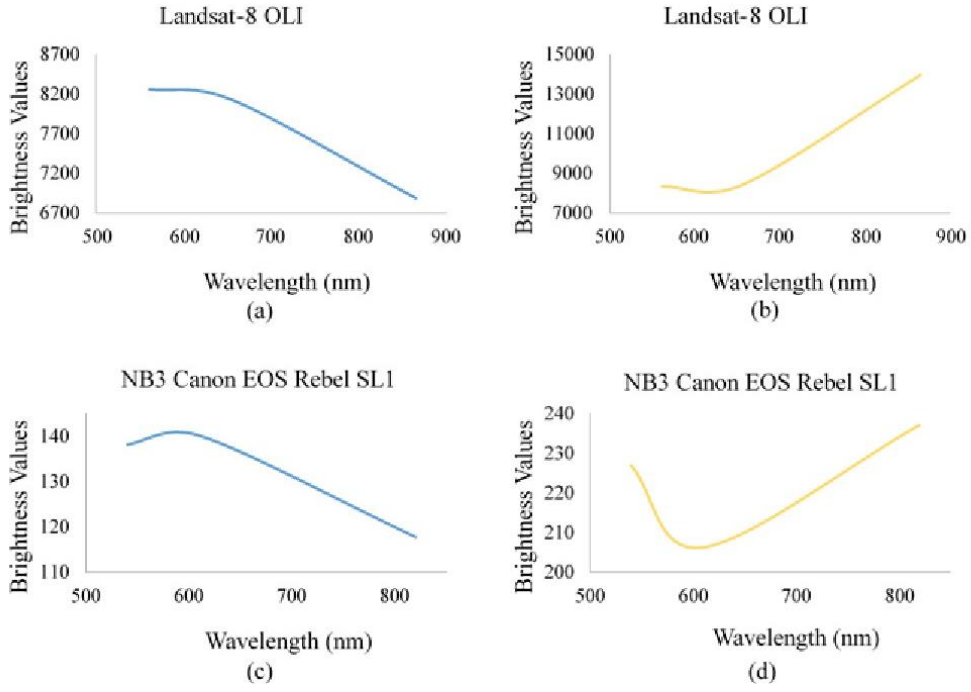

Figure 3.4 Water and Vegetation Spectral Response

Spectral response comparison between Landsat-8 and NB3: (a) OLI water and (b) OLI vegetation vs. (c) Canon EOS Rebel SL1 water and (d) Canon EOS Rebel SL1 vegetation.

3.3 Radiometric Resolution

Radiometric resolutions for the original Landsat-8 OLI and NB3 Canon EOS Rebel SL1 were calibrated to a 16-bit and 8-bit quantization levels, respectively. Table 3.3 presents the radiometric comparison of the data collected from the OLI and Canon EOS Rebel SL1 sensors and the land water threshold values based on the natural breaks with Jenks Optimization classification method. The pixel value ranges are indicative of the full extent collected NIR imagery data from the Landsat-8 OLI and NB3 Canon EOS Rebel SL1.

Table 3.3 Radiometric Data of Landsat-8 (16-bit) vs. NB3 (8-bit)

Platform	Dates	Pixel Values	Threshold Values
UAS NB-3	3/19/2015	42 - 255	157
Landsat-8	3/27/2015	5,932 - 16,462	10,805
UAS NB-3	3/16/2015	67 - 255	163
Landsat-8	3/27/2015	5,664 - 15,898	10,962
UAS NB-3	12/18/2014	75 - 255	186
Landsat-8	1/6/2015	5,365 - 12,692	8,382
UAS NB-3	12/16/2014	01 - 255	128
Landsat-8	1/6/2014	5,659 - 16,685	7,562

CHAPTER IV

DISCUSSION

4.1 Land-Water Masks

Analyzing the imagery in the full extent (Figure 3.1) versus the AOI (Figure 3.2) exposes the strengths of higher spatial resolution of the NB3 Canon EOS Rebel SL1. The full extent land-water masks show a slight difference over a more expansive coverage area than that of the AOI masks. Overall, the results consistently yielded more detailed and distinct characteristic of the AOI land-water masks, which was expected when comparing 0.05 m and 30 m spatial resolution of the NB3 Canon EOS Rebel SL1 and Landsat-8 OLI, respectively. However, the difference in spatial resolution is one of the main focuses in this research. The primary objective of this research was to compare a trending remote sensing platform, presented as UAS NB3, with reliable satellite technology, such as Landsat-8. The results from the AOI land-water masks created a more visual distinction for areas of suggested land and water, opposed to that of landsat-8 OLI relatively coarse resolution.

4.2 Statistical Comparisons

The statistical comparisons indicated a few major differences in the land-water masks generated from the Canon EOS Rebel SL1 and OLI imagery. Primarily, the distinct disagreements found in the AOI land-water-masks were not enough to result in an overall average difference greater than 1.77% of either land or water between the

comparisons. Relatively coarse spatial resolution from the OLI appeared to completely disregard areas of water suggested by the Canon EOS Rebel SL1. The March 16th Canon EOS Rebel SL1 data vs. the March 27th OLI data had the largest difference between all AOI comparisons with a 20.41%. This substantial difference was likely due to smaller scattered areas of land and water found in the March 16th comparison, opposed to the relatively more uniform areas of land and water found in the other AOI comparisons. The March 16th comparison suggests a weakness of the 30 m spatial resolution in smaller sporadic areas of land and water when analyzing the NIR imagery, land water masks, and histograms, as shown in Figure 4.1. There exists a noticeable visual difference between Figures 9a vs. 9d and Figures 9b vs. 9e. The visual difference is confirmed with the comparisons of the histograms in Figure 4.1c vs. 4.1f. The histogram for the Canon EOS Rebel SL1 shows a substantial lesser amount of water pixels relative to the OLI histogram.

The major difficulty in concluding results from this statistical comparison is due to the lack of an accurate ground truth in this research. However, in a localized research parameter, such as described in this research, the absence of a ground truth is unavoidable due to the highly dynamic water levels caused by temporal tidal variances within the LPRB. Contrarily, the temporal differences between the NB3 Canon EOS Rebel SL1 and Landsat-8 OLI should be omitted with respect to seasonal variations, as neither of the ΔDays presented in Table 2.2 and Table 2.3 were large enough to alter the absorptivity or reflectivity of the localized research parameter.

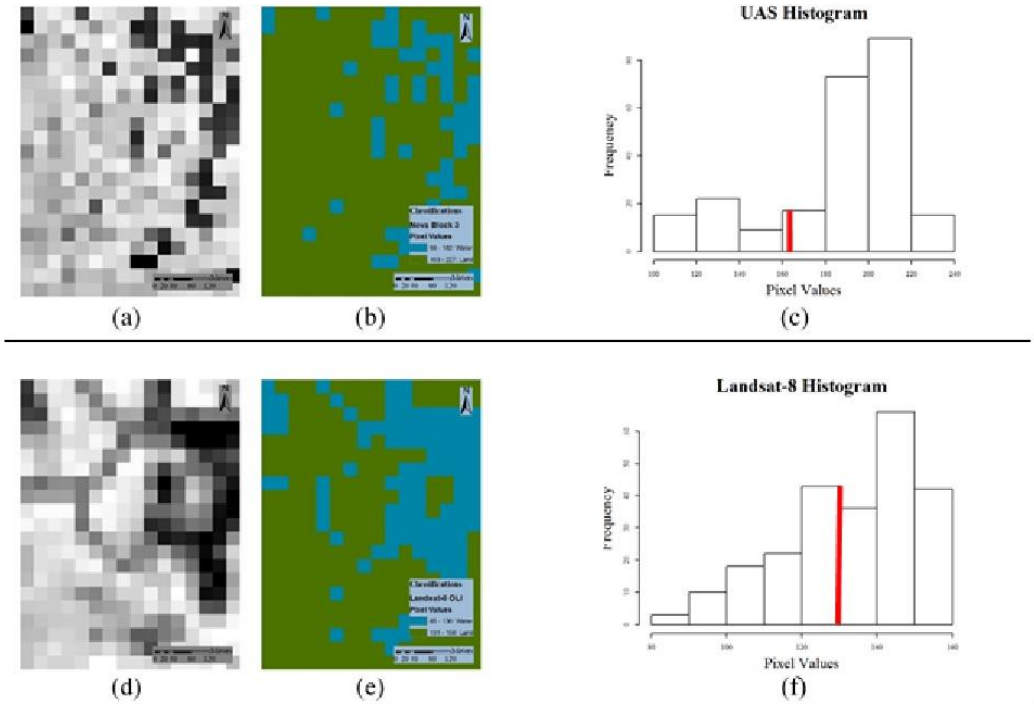

Figure 4.1 Imagery and Histogram Comparisons

(a-c) AOI Canon EOS and (d-f) OLI comparisons: (a) Mar. 16th NIR imagery, (b) land-water mask, and (c) histogram vs. (d) Mar. 27th NIR imagery, (e) land-water mask, and (f) histogram. The vertical red line on histograms (c) and (f) represents the threshold between water and land.

The spatial alignment of the imagery between Landsat-8 OLI and NB3 Canon EOS Rebel SL1 suggests a high agreement for three of the comparisons with a matched percentage range of 87.50% - 96.25%. The imagery that had a relatively low matched percentage of 67.92% was the comparison between March 27th Landsat-8 OLI vs. March 16th NB3 Canon EOS Rebel SL1. An explanation for this anomaly is presented in Figure 3.1; whereas, the March 16th land water mask comparison shows sporadic areas of water, opposed to the more uniform areas of water found in the other three land water mask comparisons. The likely reason for this substantially lower spatially aligned percentage is the 30 m spatial resolution used in the AOI imagery comparison. Higher spatial

resolution would be more effective in accurately classifying land vs. water in areas with sporadic tributaries and pools of water.

4.3 Remote Sensing Resolutions

To obtain temporally precise statistical comparisons between NB3 and Landsat-8, or any remote sensing methods, future research would benefit from simultaneously collecting data. A caveat with the stated potential future research is the orbital position of Landsat-8, which remotely senses from above the Lifted Condensation Level (LCL), making the sought after data susceptible to cloud interference. The NB3 operates below 243 m AGL, which is likely below the LCL on a mission scheduled day.

Spectrally, there was only a single band used in this research to compare classifications of land and water. The NIR wavelength was selected for its ability to measure the absorption and reflectance of total radiance between land and water. The NB3 Canon EOS Rebel SL1 used a longpass filter to attenuate the blue band in order to measure the optimal peak of reflectance in the NIR wavelength. Using the FWHM method, this research determined that the NB3 Canon EOS Rebel SL1 had an optimal NIR wavelength between 792 – 873 nm and the Landsat-8 OLI had a narrower range between 850 – 880 nm. The major benefit of operating the NB3 for aerial imagery over the localized research parameter is the capability of interchanging the sensor onboard the platform. Such a procedure occurred on the NB3 during a research mission that involved the installation of a 5-band sensor onboard the NB3 for LPRB aerial imaging. The orbiting location of Landsat-8 does not allow the OLI or TIRS to be interchanged with any other sensor.

The sensitivity difference of the two platforms did not appear to cause a substantial difference in the full-extent or AOI land-water masks comparisons. Downsampling from 16-bit to 8-bit was accomplished to ensure an unbiased comparison between the two platforms. Temporally, the comparisons were as closely matched as possible in this research. The largest difference between any of the comparisons was 21 days. The Landsat-8 satellite remotely senses an area every 16 days at a fixed orbit, opposed to the two-month return of the NB3 research schedule. However, the UAS technology used in this research has the ability to launch at variable times. Future research would benefit from scheduling a UAS to measure an area at the same time period over the course of a multi-day research trip.

CHAPTER V

CONCLUSION

Unmanned Aerial Systems are thought of as a modern aviation technology; however, research shows its genesis dates back to the early 1900s. Over the past century, UAS technology has evolved beyond vast military operations into many fields including meteorology, hydrology, ecology, etc. As a result, many government agencies have begun employing UAS technology to remotely sense areas similar to the localized research parameter studied in this project.

Since its inception in 1972, the Landsat program has exemplified a persistent history of operationally imaging the Earth's surface with the ability to collect data over a large coverage area. Many fields within geosciences have benefitted from the reliable remote sensing data collection that Landsat has made available free to the public. The latest operational design, Landsat-8, reached a milestone in the Landsat program with its Operational Land Imager (OLI) and pushbroom sensor technology, which increases its signal-to-noise ratio. The newly designed OLI remote senses in the NIR (band 5) with a wavelength of 850-880 nm, which is narrower than its predecessor's Landsat-7 ETM^{+}.

The NIR wavelength has ideal absorptivity and reflectivity properties to classify areas of water and land. The main methods of comparing imagery with land-water masks and statistical comparisons, utilizes the DN from the collected NIR data, which results in

BVs. Land-water masks in this research were created using a single spectral band from each remote sensing platform; Landsat-8 OLI and NB3 Canon Rebel EOS SL1.

The NB3 Canon EOS Rebel SL1 was superior to the Landsat-8 OLI for classifying water vs. land over time in the localized research parameter within the LPRB. A major benefit of the NB3 is its operating altitude of 243 m AGL, opposed to Landsat-8 orbiting at 7.05 x 10^5 m AGL. The NB3 operated entirely under the LCL; therefore, was not susceptible to faulty data due to cloud interference. Contrarily, Landsat-8 OLI collected faulty data over the LPRB on December 21st, 2014; which would have been a closer dated match to the NB3 research schedule. Due to the cloudy Landsat OLI imagery from December 21st, 2014, shown in Figure 5.1, this research used Landsat-8 OLI January 06th, 2015 data to compare with the data collected on December 16th and 18th, 2014 from the NB3 Canon EOS Rebel SL1.

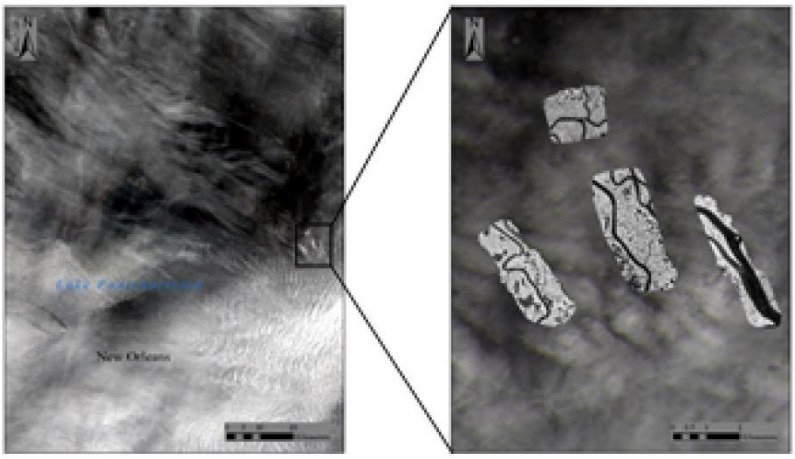

Figure 5.1 Cloud Interference

Dec. 21st Landsat-8 OLI imagery of (a) the New Orleans area and (b) the localized research parameter with NB3 Canon EOS Rebel SL1 NIR imagery overlay.

Another advantage of the UAS over Landsat-8 is the capability to operate different sensors onboard the UAS platform. In this research the NB3 Canon EOS Rebel SL1 was used with a Kodak Wratten #12 deep yellow filter to attenuate all wavelengths less than 500 nm. This was an optional equipment addition to the NB3 platform. Landsat-8 does not have the capability to interchange an onboard sensor due to its orbiting location. A benefit of the Landsat-8 OLI data is its no-cost availability to the public. This research selected Landsat-8 OLI for its reliable record and no-cost data downloads. Other high-resolution satellites such as GeoEye-1, WorldView-3, or QuickBird could have been selected to compare against the NB3 Canon EOS Rebel SL1; however, these satellites offer collected data downloads at an expensive cost. Additionally, Landsat-8 OLI was designed as a linear array pushbroom sensor, and the NB3 Canon EOS Rebel SL1 was designed as a digital frame camera area array sensor. Pushbroom sensors operate by sensing an entire row simultaneously with multiple detectors per channel. An area array sensor captures an entire image with overlapping frames.

The persistent advancement of UAS technology for geoscience applications will benefit a localized research parameter such as described in this research. Landsat-8 will have the greatest impact by continuing large-scale global imaging, where 30 m resolution is sufficient.

REFERENCES

Colwell, R. N., 1997, "History and Place of Photographic Interpretation," in *Manual of Photographic Interpretation*, 2nd Ed., W.R. Phillipson (Ed.), Bethesda: ASPRS, 33-48.

Cress, B. J., Hutt, M., Sloan, J., Bauer, M., Feller, M., Goplen, S., … Survey, U. S. G. (2015). U . S . Geological Survey Unmanned Aircraft Systems (UAS) Roadmap 2014.

Dash, P., Gottsche, F.M., Olesen, F.S., Fischer, H., 2002. Land surface temperature and emissivity estimation from passive sensor data: theory and practice-current trends. International Journal Remote Sensing 23:2563–2594, doi: http://dx.doi.org/10.1080/01431160110115041

J. Everaerts. (2008). The use of unmanned aerial vehicles (uavs) for remote sensing and mapping. *The International Archives of the Photogrammetry, Remote Sensing and Spatial Information Sciences*, *XXXVII*, 1187–1192.

Gimenes, R. A. V, Vismari, L. F., Avelino, V. F., Camargo, J. B., Almeida, J. R. De, & Paulo, J. (2014). Guidelines for the Integration of Autonomous UAS into the Global ATM, 465–478. doi:10.1007/s10846-013-9945-0

Gupta, S., Ghonge, M., & Jawandhiya, P. (2013). Review of Unmanned Aircraft System (UAS). *International Journal of Advanced Research in Computer Engineering & Technology (IJARCET)*, *2*(4), 1646–1658. Retrieved from http://www.researchgate.net/publication/249998592_Review_of_Unmanned_Aircraft_System_(UAS)/file/72e7e51e8ef1668ce8.pdf

Hugenholtz, C. (2012). Small unmanned aircraft systems for remote sensing and earth science research. *Eos*, *93*(25), 24–25. doi:10.1117/1.3474649.

Jensen, John R. Remote Sensing of the Environment: An Earth Resource Perspective. Upper Saddle River, NJ: Pearson Prentice Hall, 2007. Print.

Kantha, L. (2013). Classification of hurricanes: Lessons from Katrina, Ike, Irene, Isaac and Sandy. *Ocean Engineering*, *70*, 124–128. doi:10.1016/j.oceaneng.2013.06.007

Knight, E., & Kvaran, G. (2014). Landsat-8 Operational Land Imager Design, Characterization and Performance. *Remote Sensing*, *6*(11), 10286–10305. doi:10.3390/rs61110286

Li, P., Jiang, L., & Feng, Z. (2013). Cross-comparison of vegetation indices derived from landsat-7 enhanced thematic mapper plus (ETM+) and landsat-8 operational land imager (OLI) sensors. *Remote Sensing*, *6*(1), 310–329. doi:10.3390/rs6010310

Moorhead, Robert, Robbie Hood, and John Coffey. Optimal Unmanned Aerial Systems River Observing Strategy Workshop. Workshop. Boulder: Mississippi State U and NOAA UAS Program Office, 2012. Print.

Murray, Alan T., and Tung-Kai Shyy. "Integrating Attribute and Space Characteristics in Choropleth Display and Spatial Data Mining." International Journal of Geographical Information Science 14.7 (2000): 649-67. Web.

National Aeronautics and Space Administration, 2010, About MODIS: accessed December 7, 2010, at http://modis.gsfc.nasa.gov/about/.

NOAA Tropical Cyclone Report, 2013

Roy, D. P., Wulder, M. a., Loveland, T. R., C.E., W., Allen, R. G., Anderson, M. C., … Zhu, Z. (2014). Landsat-8: Science and product vision for terrestrial global change research. *Remote Sensing of Environment*, *145*, 154–172. doi:10.1016/j.rse.2014.02.001

Reuter, D., Richardson, C., Pellerano, F., Irons, J., Allen, R., Anderson, M., … Thome, K. (2015). The Thermal Infrared Sensor (TIRS) on Landsat 8: Design Overview and Pre-Launch Characterization. *Remote Sensing*, *7*(1), 1135–1153. doi:10.3390/rs70101135Schmugge, T. J., Kustas, W. P., Ritchie, J. C., Jackson, T. J., & Rango, A. (2002). Remote sensing in hydrology. *Advances in Water Resources*, *25*(8-12), 1367–1385.

Spriesterbach, T. P., Bruns, K. a., Baron, L. I., & Sohlke, J. E. (2013). Unmanned aircraft system airspace integration in the national airspace using a ground-based sense and avoid system. *Johns Hopkins APL Technical Digest (Applied Physics Laboratory)*, *32*(3), 572–583.

United States of America. FAA, DOT. By Michael P. Huerta and Anthony R. Foxx. N.p., 15 Feb. 2015. Web. 25 June 2015. <https://www.faa.gov/regulations_policies/rulemaking/recently_published/media/2120-AJ60_NPRM_2-15-2015_joint_signature.pdf>. Notice of Proposed Rulemaking (NPRM). Billing Code 4910-13-P [Docket No.: FAA-2015-0150; Notice No. 15-01] RIN 2120–AJ60

Watts, A. C., Ambrosia, V. G., & Hinkley, E. A. (2012). Unmanned Aircraft Systems in Remote Sensing and Scientific Research: Classification and Considerations of Use. *Remote Sensing*, *4*(12), 1671–1692. doi:10.3390/rs4061671

Whitehead, K., Hugenholtz, C. H., Myshak, S., Brown, O., LeClair, A., Tamminga, A., … Eaton, B. (2014). Remote sensing of the environment with small unmanned aircraft systems (UASs), part 2: scientific and commercial applications 1. *Journal of Unmanned Vehicle Systems*, *02*(03), 86–102. doi:10.1139/juvs-2014-0007